Arabian Journal of Chemistry (2018) xxx, xxx–xxx

King Saud University

Arabian Journal of Chemistry

www.ksu.edu.sa
www.sciencedirect.com

ORIGINAL ARTICLE

Optimization and detailed stability study on coupling of $CdMoO_4$ into $BaWO_4$ for enhanced photodegradation and removal of organic contaminant

Mohammad Eghbali-Arani [a,*], Saeid Pourmasoud [a], Farhad Ahmadi [b], Mehdi Rahimi-Nasrabadi [c,d], Vahid Ameri [e], Ali Sobhani-Nasab [f,*]

[a] *Department of Physics, University of Kashan, Kashan, Iran*
[b] *Department of Medicinal Chemistry, School of Pharmacy-International Campus, Iran University of Medical Sciences, Tehran, Iran*
[c] *Chemical Injuries Research Center, Baqiyatallah University of Medical Sciences, Tehran, Iran*
[d] *Department of Chemistry, Faculty of Pharmacy, Baqiyatallah University of Medical Sciences, Tehran, Iran*
[e] *Department of Physics, Faculty of Science, University of Hormozgan, Bandar-Abbas, Iran*
[f] *Young Researchers and Elites Club, Arak Branch, Islamic Azad University, Arak, Iran*

Received 21 February 2018; accepted 16 May 2018

KEYWORDS

$BaWO_4/CdMoO_4$;
Visible light;
Nanocomposites;
Eco-friendly method

Abstract $BaWO_4$ nanoparticles and $BaWO_4/CdMoO_4$ nanocomposites were synthesized by eco-friendly method at low temperature. The effects of various capping agents such as glucose, fructose, lactose, and starch on the morphology and particle size of $BaWO_4/CdMoO_4$ nanocomposites were investigated. The nanocluster was obtained with glucose and Ba^{2+} to capping agent molar ratio of (1:2). $BaWO_4/CdMoO_4$ nanocomposites were analyzed through techniques including, XRD, FT-IR, VSM, TEM, PL, FESEM, UV–vis, and EDX. According to the BET results, in the presence of glucose as the capping agent, surface area increased from 13.781 m_2/g to 122.22 m_2/g. Furthermore, adding $CdMoO_4$ nanoparticles to $BaWO_4$ causes optical properties and photocatalytic activity of $BaWO_4$ to improve. Moreover, the effects of several factors such as $BaWO_4/CdMoO_4$ nanocomposites concentration and its particle size and difference dyes on the photocatalytic performance of $BaWO_4/CdMoO_4$ nanocomposites were studied under visible light.

* Corresponding authors.
E-mail addresses: m.eghbali@kashanu.ac.ir (M. Eghbali-Arani), Ali.sobhaninasab@gmail.com (A. Sobhani-Nasab).
Peer review under responsibility of King Saud University.

Production and hosting by Elsevier

1. Introduction

Dye is one of the most important chemicals applied in many industries such as paint, food and furniture. However, it can be considered as a real threat to the environment. Synthetic dyes are main pollutant of wastewater. Up to now, extensive

https://doi.org/10.1016/j.arabjc.2018.05.007
1878-5352 © 2018 Production and hosting by Elsevier B.V. on behalf of King Saud University.

research has been carried out to decrease concentration of organic dyes in wastewater (Zhong et al., 2012; Zhu et al., 2018a; Dutta et al., 2009; Ozer et al., 2007; Fan et al., 2009). Several methods have been developed to synthesize photocatalysts including reverse-microemulsion process (Mi et al., 2009); solvothermal synthesis (Zhang et al., 2006), microwave assisted citrated complex (Ryu et al., 2005), combustion synthesis (Xia et al., 2001), solid-state reaction (Pupp et al., 1969), complex capping agentization (de Azevedo Marques et al., 2006), molten salt route (Afanasiev, 2007), and electrochemical method (Sun et al., 2011). Nowadays, tungstates and molybdates have received much attention due to their application in many fields involving humidity sensors, catalysts, solid states lasers, microwave applications, photoluminescent devices, and so on. They have scheelite-type tetragonal structure. Each X atom (X = Mo and W) is surrounded by four equivalent O atoms consisting the $[XO_4]^2$ tetrahedral configuration and every divalent metal shares corners with eight oxygen atoms of $[XO_4]^2$ tetrahedrons (Kongsinlark et al., 2012; Joshi et al., 2014). $BaWO_4$ has been extensively used as catalysts with good efficiency for the photodegredation of organic pollutants. Despite the fact that $BaWO_4$ is a well-known photocatalyst, it has two important problems. Firstly, this semiconductor is active under UV (Wei et al., 2010; Sathishkumar et al., 2011). Secondly, fast recombination and disappearance of photogenerated electron-hole (e-h) pairs in $BaWO_4$ can reduce the effective degredation of pollutants (Ahmadi et al., 2018). Therefore, a tremendous effort has been made to tackle these problems. There are two significant methods to enhance the photocatalytic efficiency of $BaWO_4$. One refers to the coupling of two semiconductors and the other is to add metal ion dopants as modifier into the matrix of $BaWO_4$ (Safardoust-Hojaghan and Salavati-Niasari, 2017). The aim of this study is to synthesize $BaWO_4/CdMoO_4$ nanocomposites at low temperature by the co-precipitation process and investigate its photocatalytic properties of final products under visible light. In addition to this, the effects of solution pH and photocatalyst loading were considered as well. To the best of our knowledge, this is a first report on the preparation of $BaWO_4/CdMoO_4$ nanocomposites. Using glucose, fructose, lactose, and starch with the Ba^{2+} to capping agent molar ratios of (1:1) and (1:2), can be considered as the novelty of the preparation of $BaWO_4/CdMoO_4$ nanocomposites. As the obtained nanocomposite was studied by scanning electron microscopy, Fourier transforms infrared spectroscopy, vibrating sample magnetometer, X-ray diffraction, Brunauer–Emmett–Teller (BET), UV–visible absorption, and X ray energy dispersive spectroscopy.

2. Experimental

2.1. Synthesis of $BaWO_4$ nanoparticles

At first, 1 mmol of $Ba(NO_3)_2.4H_2O$ was dissolved in 20 ml of distilled water, which we called it solution A. Then, 1 mmol of $Na_2WO_4{\cdot}H_2O$ and 3 mmol of capping agent were dissolved in 30 mL of distilled water and mixed together to form solution B. Afterwards, solutions A and B were mixed under constant stirring for 45 min at room temperature. Finally, the precipitation was centrifuged and dried at room temperature.

2.2. Synthesis of $BaWO_4/CdMoO_4$ nanocomposite

$BaWO_4/CdMoO_4$ nanocomposites were prepared by co-precipitation method. $Ba(NO_3)_2{\cdot}4H_2O$ and green capping agents with different molar ratios were dissolved in 30 ml of distilled water (solution A). The solution B was formed by adding 1 mmol of $Na_2WO_4{\cdot}H_2O$ to 30 mL of distilled water. Then, solution A was added into solution B under vigorous stirring to make solution C. Subsequently, two solutions containing 1 mmol of $Cd(CH_3CO_2)_2$ and $(NH_4)_6Mo_7O_{24}.4H_2O$ was added to solution C under constant stirring. Finally, the obtained precipitation was washed three times with distilled water and dried out at 25 °C for 3 h. Synthesis pathway of the $BaWO_4/CdMoO_4$ nanocomposites is shown in Scheme 1. All reaction conditions are listed in Table 1.

2.3. Materials and physical measurements

All of the chemicals used in synthesis of $BaWO_4/CdMoO_4$ nanocomposites including $Ba(NO_3)_2{\cdot}4H_2O$, $Na_2WO_4{\cdot}H_2O$, $Cd(CH_3CO_2)_2$, $(NH_4)_6Mo_7O_{24}.4H_2O$, glucose, fructose, lactose, and starch were purchased from Merck Company and didn't purify any more. The XRD patterns were recorded by a Philips-X'pertpro, X-ray diffractometer using Ni-filtered Cu Ka radiation. Fourier transform infrared (FT-IR) spectra were recorded on Nicolet Magna- 550 spectrometer in KBr pellets. Scanning electron microscopy (SEM) images were obtained on LEO-1455VP equipped with an energy dispersive X-ray spectroscopy. The EDX analysis with 20 kV accelerated voltage was done. Transmission electron microscopy (TEM) image was found by a Philips EM208 transmission electron microscope with an accelerating voltage of 200 kV. The diffused reflectance UV–visible spectrums (DRS) of the samples, were recorded by the V-670 UV–Vis Spectrophotometer (Jasco). The magnetic measurements of samples were carried out in a vibrating sample magnetometer (VSM) (Meghnatis Daghigh Kavir Co., Kashan Kavir, Iran) at room temperature in an applied magnetic field sweeping between ±10,000 Oe.

2.4. Photocatalytic measurements

The photocatalytic ability of $BaWO_4/CdMoO_4$ nanocomposites in the presence of varied dyes was measured. The degradation reaction was conducted in a quartz photocatalytic reactor. The photocatalytic degradation was carried out with 5×10^{-5} M of solutions containing 0.05 g of nanocomposites. The mixture was aerated for 30 min, and it was positioned in the photoreactor in which the vessel was 20 cm away from the light source (a 400 W Osram lamp). The mixture was aliquoted in periodic intervals during the irradiation, and previous to be analyzed with the UV–Vis spectrometer, it was centrifuged. The percentage of dyes degradation was evaluated through the following formula:

$$\textit{Degradation rate}\ (\%) = \frac{100(C_0 - C_t)}{C_0} \quad (1)$$

where C_0 and C_t are the absorbance value of solution at 0 and t min, respectively.

Please cite this article in press as: Eghbali-Arani, M. et al., Optimization and detailed stability study on coupling of $CdMoO_4$ into $BaWO_4$ for enhanced photodegradation and removal of organic contaminant. Arabian Journal of Chemistry (2018), https://doi.org/10.1016/j.arabjc.2018.05.007

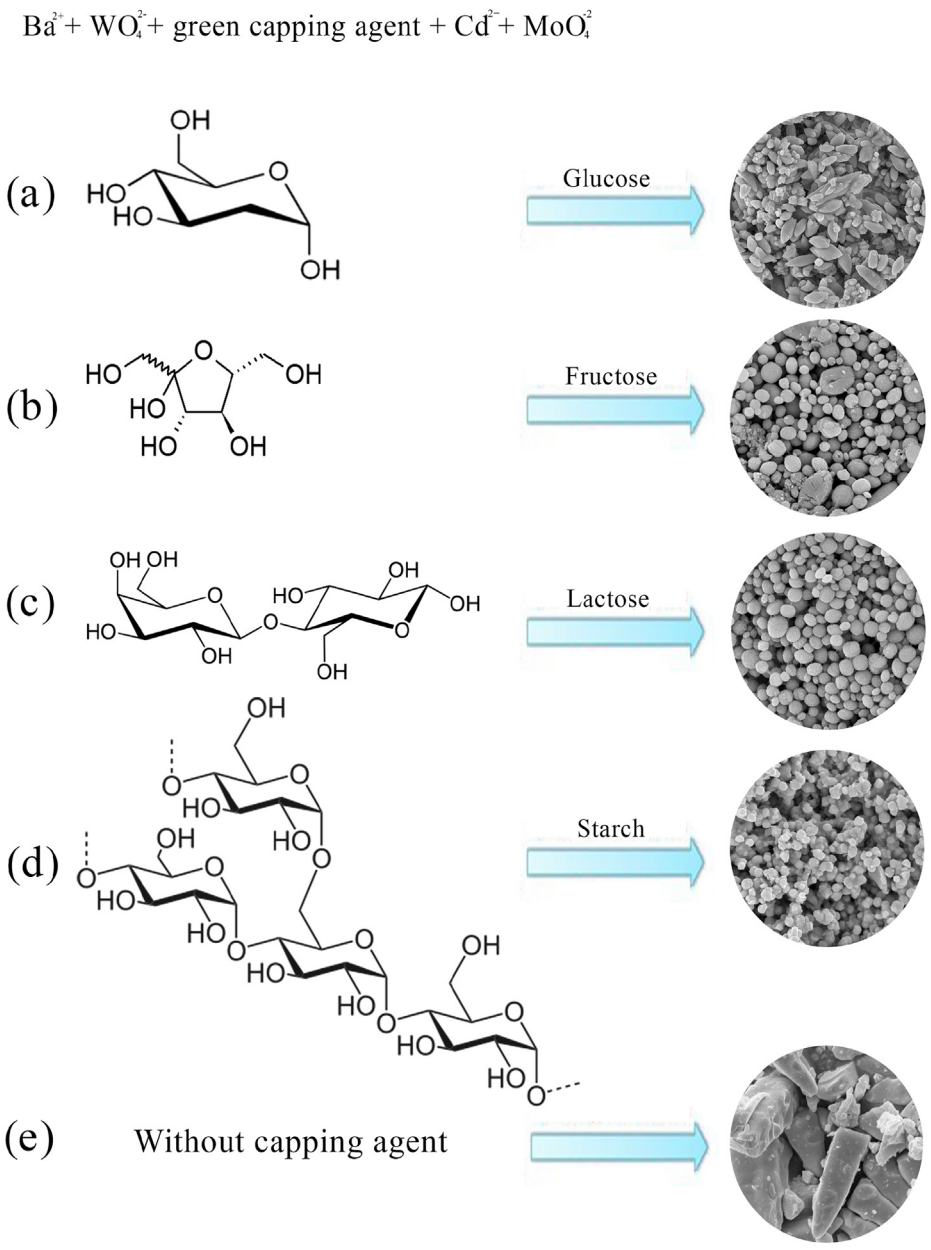

Scheme 1 Schematic the effects of capping agents and their different ratio on the size of final products.

Table 1 The preparation conditions of the $BaWO_4$ nanostructures and $BaWO_4/CdMoO_4$ nanocomposites.

Sample no	Capping agents	Molar ratio (M: Capping agents)	Temperature °C	Product	Debye–Scherrer crystallite size (nm)	Figure of SEM images
1	Glucose	(1:2)	25	$BaWO_4$	21.1	–
2	–	–	25	$BaWO_4/CdMoO_4$	36.7	Fig. 3a
3	Glucose	(1:1)	25	$BaWO_4/CdMoO_4$	31.5	Fig. 3b
4	Fructose	(1:1)	25	$BaWO_4/CdMoO_4$	32.7	Fig. 3c
5	Lactose	(1:1)	25	$BaWO_4/CdMoO_4$	29.8	Fig. 3d
6	Starch	(1:1)	25	$BaWO_4/CdMoO_4$	30.6	Fig. 3e
7	Glucose	(1:2)	25	$BaWO_4/CdMoO_4$	24.6	Fig. 4a
8	Fructose	(1:2)	25	$BaWO_4/CdMoO_4$	25.8	Fig. 4b
9	Lactose	(1:2)	25	$BaWO_4/CdMoO_4$	25.6	Fig. 4c
10	Starch	(1:2)	25	$BaWO_4/CdMoO_4$	25.3	Fig. 4d

3. Results and discussion

XRD patterns of $BaWO_4$ nanostructures are shown in Fig. 1a. The spectrum of bare $BaWO_4$ sample shows a series of diffraction peaks at the position of 26.32° ((112) line), 32.18° ((002) line), 43.18° ((200) line), and 54.63° ((222) line) which is in good agreement with the standard JCPDS file of $BaWO_4$ tetragonal phase (space group I41/a, JCPDS No. 85-0588). The XRD patterns of $BaWO_4/CdMoO_4$ nanocomposites with different parameters such as molar ratio and capping agent have been displayed in Fig. 1a–j, correspondingly. As our results suggest, all prepared nanocomposites are pure and have two phases. The first is the phase of $BaWO_4$ and $CdMoO_4$ with crystal structure of tetragonal (JCPDS 85-0588) and space group of I41/amd and the second is tetragonal (JCPDS 85-0888) with space group of I41/a, respectively. From XRD data and Scherrer equation the crystallite diameter (Dc) of $BaWO_4$ nanostructures and $BaWO_4/CdMoO_4$ nanocomposites, samples 1–10, calculate to be 21.1, 36.7, 31.5, 32.7, 29.8, 30.6, 24.6, 25.8, 25.6 and 25.3 nm, respectively (Javidan et al., 2015).

$$Dc = \frac{K\lambda}{\beta \cos\theta} \tag{2}$$

In which β is the breadth of the noticed diffraction line at its half intensity maximum, K is the so-called shape factor, which commonly takes a value of approximately 0.9, and λ is the wavelength of X-ray source applied in XRD. Therefore, one can simply find out that the steric hindrance of a capping agent increases with the decrease in the size of nanocomposites.

The purity of $BaWO_4/CdMoO_4$ nanocomposites was confirmed by EDS technique. As illustrated in Fig. 2 (sample No. 7), the $BaWO_4/CdMoO_4$ nanocomposites are composed of Ba, W, Cd, Mo, and O elements. Furthermore, no impurity peaks were observed which indicates high purity level of as-prepared $BaWO_4/CdMoO_4$ nanocomposites.

The reaction mechanism with capping agent can be proposed as follow:

$$7Na_2WO_4 \cdot 2H_2O + (capping\ agent) \rightarrow 14Na + +7WO_4^{2-} + (capping\ agent) + 14H_2O \tag{3}$$

$$7Ba(NO_3)_2 \cdot 4H_2O \rightarrow 7Ba^{2+} + 14NO_3^- + 28H_2O \tag{4}$$

$$7Ba^{2+} + 7WO_4^{2-} \rightarrow 7BaWO_4 \tag{5}$$

$$14Na^+ + 14NO^{3-} \rightarrow 14NH_4NO_3 \tag{6}$$

$$7Cd(CH_3COO)_2 \cdot 2H_2O \rightarrow 7Cd^{2+} + 14CH_3COO^- + 14H_2O \tag{7}$$

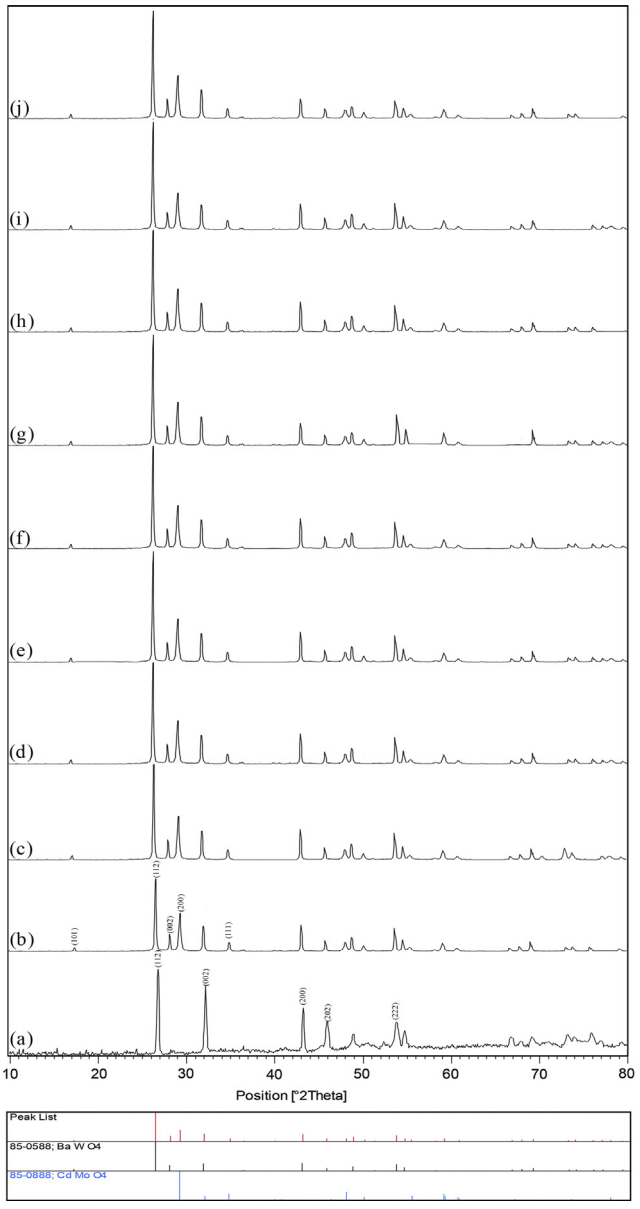

Fig. 1 XRD pattern of $BaWO_4$ obtained in the presence of (a) glucose, (b) $BaWO_4/CdMoO_4$ without capping agent, and $BaWO_4/CdMoO_4$ obtained with the Ba^{2+} to capping agent molar ratio of (1:1) in the presence of (c) glucose (d) fructose, (e) lactose and (f) starch, $BaWO_4/CdMoO_4$ obtained with the Ba^{2+} to capping agent molar ratio of (1:2) in the presence of (g) glucose (h) fructose, (i) lactose and (j) starch.

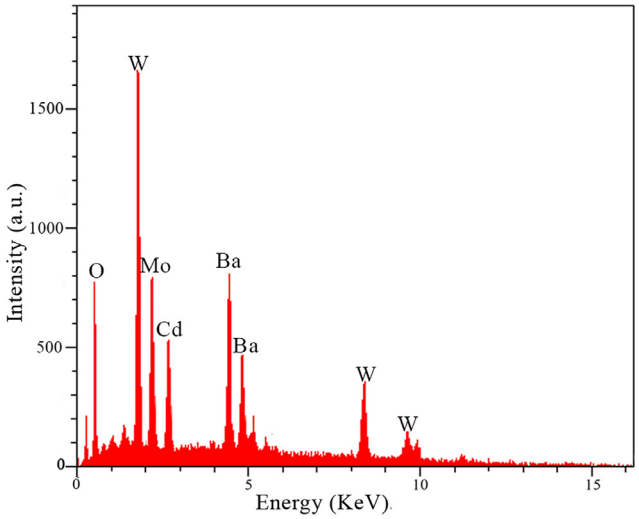

Fig. 2 EDS pattern of $BaWO_4/CdMoO_4$ nanocomposites obtained with the Ba^{2+} to capping agent molar ratio of (1:2) in the presence of glucose (Sample No. 6).

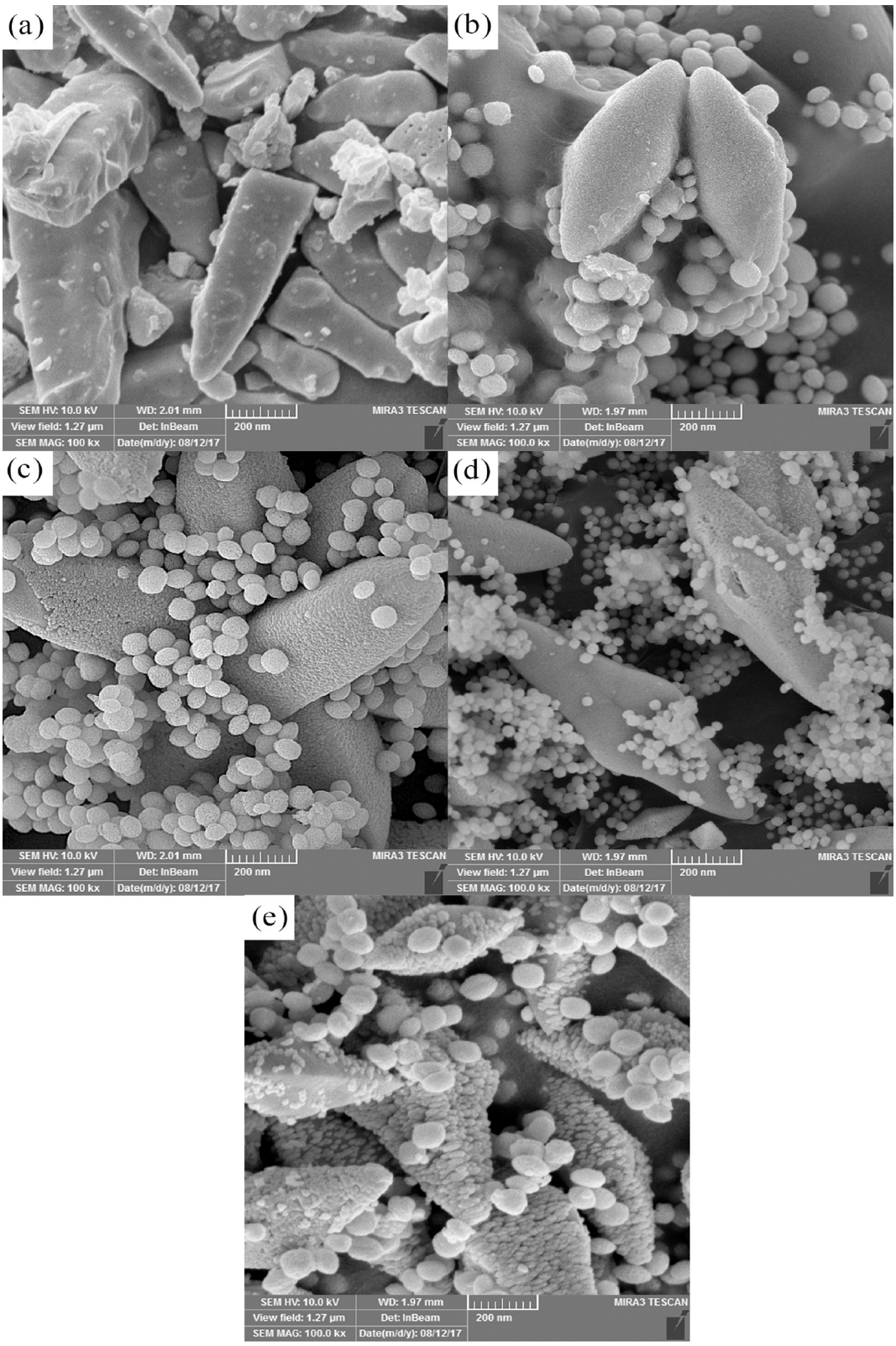

Fig. 3 SEM images of $BaWO_4/CdMoO_4$ nanocomposites obtained (a) without capping agents and with the Ba^{2+} to capping agent molar ratio of (1:1) in the presence of four different capping agents (b) glucose, (c) fructose, (d) lactose, and (e) starch.

$$(NH_4)_6Mo_7O_{24}\cdot 4H_2O + (capping\ agent) \rightarrow 6NH_4^+ + 7MoO_4^{2-} + (capping\ agent) + 8H+ \quad (8)$$

$$14CH_3COO^- + 8H^+ + 6NH_4^+ \rightarrow 14CH_3COOH \quad (9)$$

$$7Cd^{2+} + 7MoO_4^{2-} \rightarrow 7CdMoO_4 \quad (10)$$

$$7Na_2WO_4\cdot 2H_2O + 7Ba(NO_3)_2\cdot 4H_2O + 7Cd(CH_3COO)_2\cdot 2H_2O + (NH_4)_6Mo_7O_{24}\cdot 4H2O + (capping\ agent) \rightarrow 7BaWO_4/CdMoO_4 + 14NH_4NO_3 + 14CH_3COOH + (capping\ agent) + 60H_2O \quad (11)$$

Green capping agents and surfactants used in different nanoparticles synthesis procedure can cause de-agglomerate particles by reducing condensation reaction in liquid phase (Zinatloo-Ajabshir et al., 2017; Hosseinpour-Mashkani et al., 2016; Sobhani-Nasab et al., 2016). The effects of difference molar ratios of carbohydrates as green capping agents to metal (Ba^{2+}) on the size and morphology of the final products were investigated, as shown in Schematic 2. A blank test in the absence of capping agent was performed and as a result, micrometer nanocomposites were produced, as shown in Fig. 3a. Next, the different kinds of capping agents with the Ba^{2+} to capping agent molar ratio of (1:1) were employed. Furthermore, the prepared nanocomposites in the presence of glucose as a capping agent, the prepared nanoclusters were mixed with sphere-like nanoparticles. Also, the size of nanoparticles became smaller as we changed the type of capping agent (from glucose to fructose, lactose, and starch, respectively Fig. 3(b)–(e). Increasing capping agent, glucose, to Ba^{2+} molar ratio from (1:1) to (1:2) causes uniform

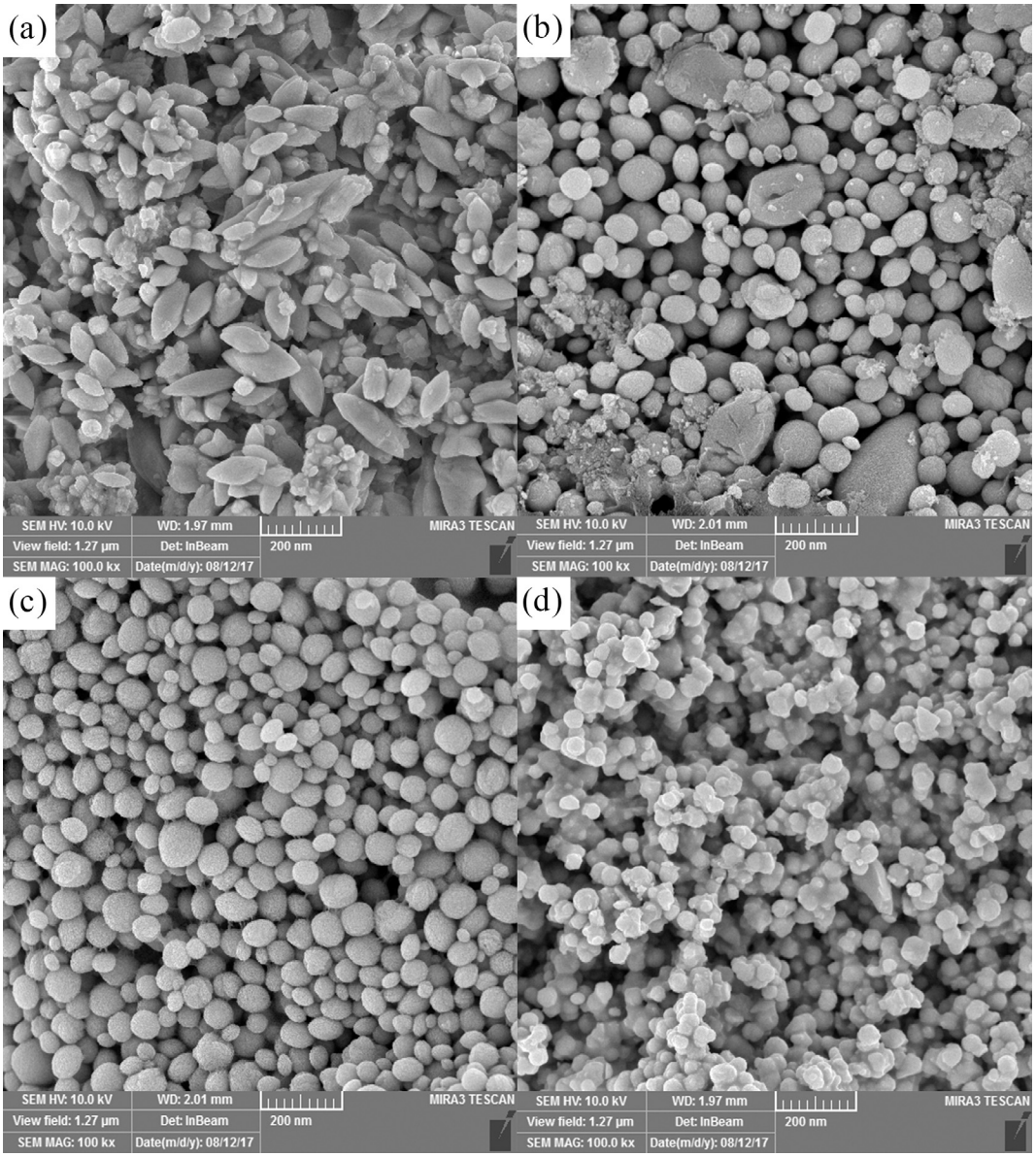

Fig. 4 SEM images of $BaWO_4/CdMoO_4$ nanocomposites obtained with the Ba^{2+} to capping agent molar ratio of (1:2) in the presence of four different capping agents (a) glucose, (b) fructose, (c) lactose, and (d) starch.

nanoclusters with appropriate size distribution to produce. Moreover, changing glucose to other capping gents causes morphology of products to change from nanoclusters to sphere-like nanoparticles Fig. 4a–d).

Transmission electron microscopy (TEM) technique was used to further examine the morphology of nanocomposites. Two typical samples of as-prepared nanocomposites in the presence of glucose and starch with the Ba^{2+} to capping agent molar ratio of (1:2) in different magnification have been depicted in Fig. 5. The as-prepared nanoclusters with the size of nearly 50–70 nm in the presence of glucose Fig. 5(a) and sphere-like nanocomposites prepared in the presence of starch have been shown in Fig. 5b, respectively.

Fig. 6a and b shows the FT-IR spectra of the $BaWO_4$ nanoparticles (sample No. 1) and $BaWO_4/CdMoO_4$ nanocomposites (sample No. 7), respectively. The characterization peaks in the $BaWO_4$ nanoparticles spectrum are 835 cm^{-1} which is attributed to vibration of atoms in tetrahedral oxygen environment; W–O at $BaWO_4$ and 824.58 cm^{-1} which is related to vibration of Ba atoms in the octahedral oxygen environment in nanosized $BaWO_4$ nanoparticles. Moreover, according to Fig. 6b, the FT-IR spectrum of $BaWO_4/CdMoO_4$ nanocomposites, bands at 876 cm^{-1} are related to the vibration of W-O at $BaWO_4$ (de Azevedo Marques et al., 2006). Besides, the characteristic peaks at 654 and 579 cm^{-1} are belong to O-Mo-O bending mode and Cd-O stretching modes, respectively. Moreover, the band located in the region 3200–3700 cm^{-1} could be attributed to the v(OH) stretching vibration of physisorbed water molecules (Sobhani-Nasab et al., 2017).

The magnetic property of $BaWO_4/CdMoO_4$ nanocomposites at 300 K is shown Fig. 7. VSM data demonstrate that as-synthesized $BaWO_4/CdMoO_4$ nanocomposites have ferromagnetic properties, and the correspondent magnetization value is nearly 0.042 emu/g.

The thermal characteristics of $BaWO_4$ nanoparticles and $BaWO_4/CdMoO_4$ nanocomposites in temperature range of 27–850 °C were examined by thermo gravimetric (TG) analysis. The graphs have been presented in Fig. 8. The TG curves

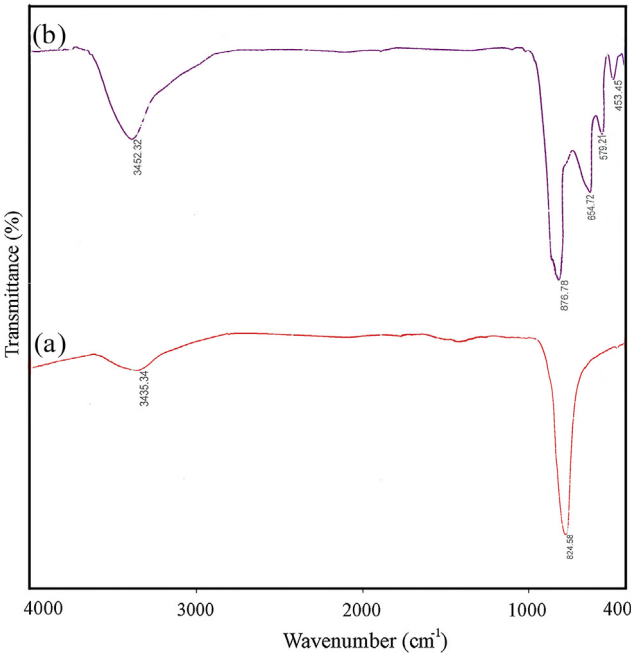

Fig. 6 FT-IR spectra of (a) $BaWO_4$ nanostructures (Sample No. 1) and (b) $BaWO_4/CdMoO_4$ nanocomposites (Sample No. 7).

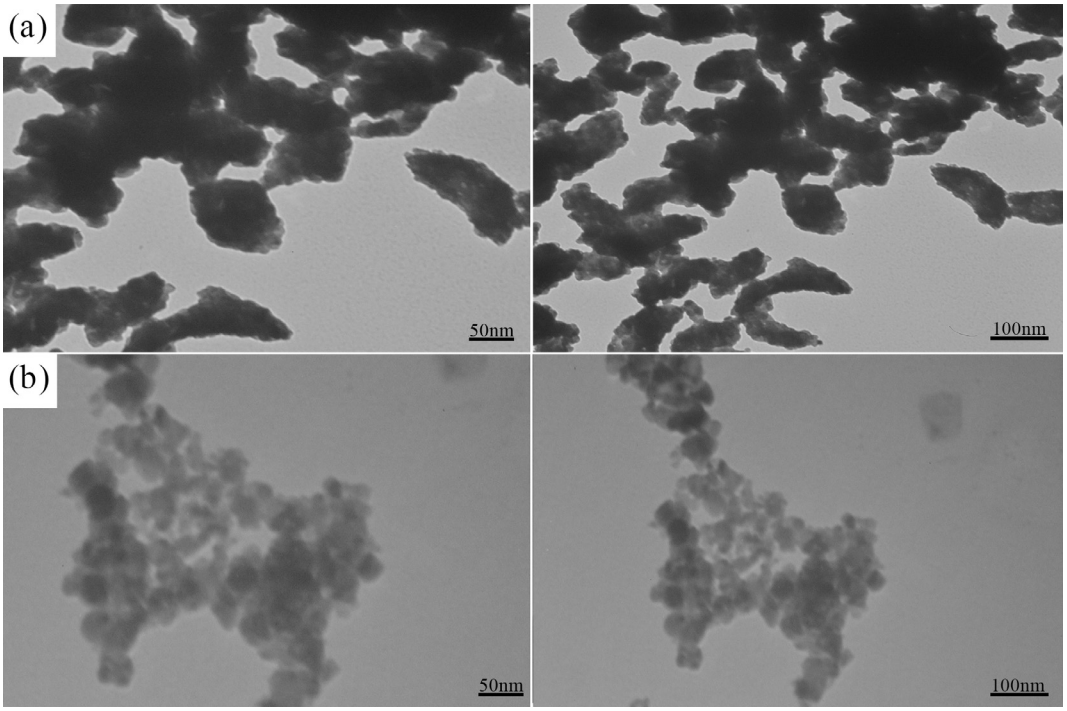

Fig. 5 TEM image of $BaWO_4/CdMoO_4$ nanocomposites obtained with the Ba^{2+} to capping agent molar ratio of (1:2) in the presence of (a) glucose, and (b) starch.

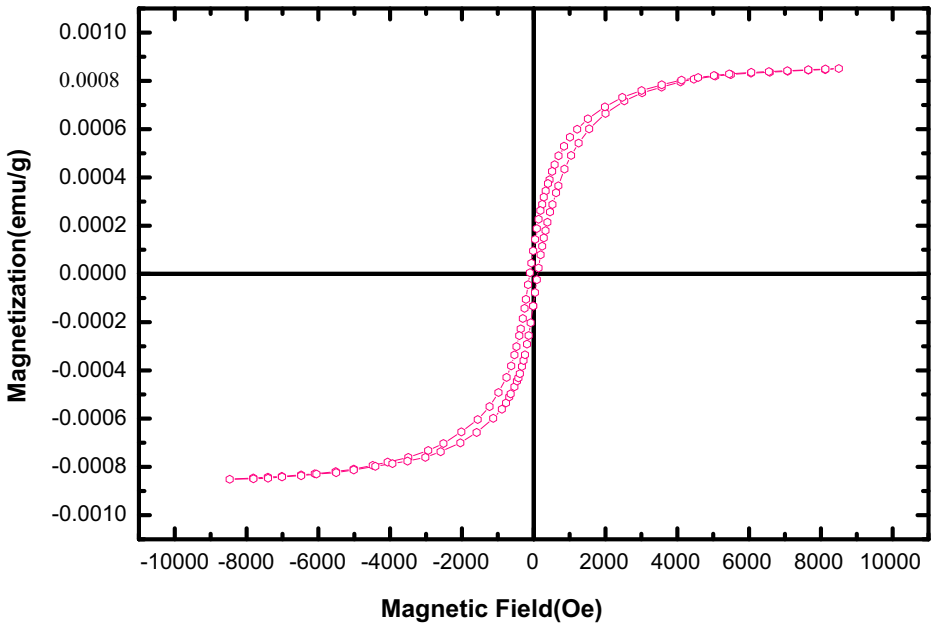

Fig. 7 VSM curve of $BaWO_4/CdMoO_4$ nanocomposites (Sample No 6).

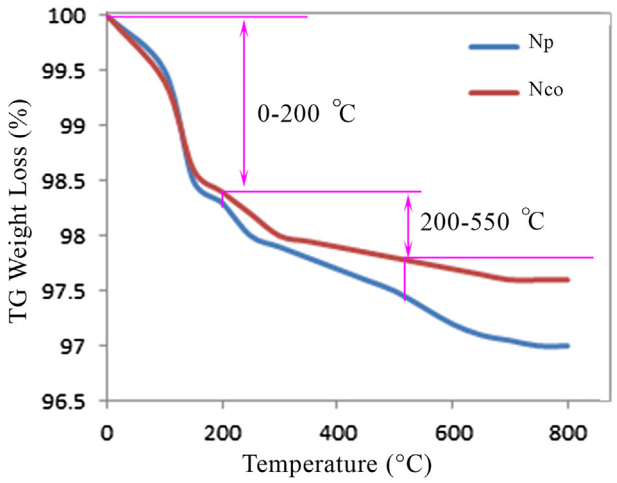

Fig. 8 Thermogravimetric profiles of $BaWO_4$ nanostructures and $BaWO_4/CdMoO_4$ nanocomposites.

of $BaWO_4$ and $BaWO_4/CdMoO_4$ nanoparticles exhibit two stages of weight loss in the temperature between 30–200 °C and 200–550 °C as well. The first stage of weight loss could be associated with water molecules, which have been physically absorbed on the surface of catalysts. The next one, could be linked with the removal of chemisorbed water molecules. The organic resides trapped inside the pores on the surface of catalyst were released in the weight loss observed between 200–550 °C. An ove 550 °C, no considerable weight loss is seen for two samples, suggesting that phase transition and crystallization do not take place in this temperature region. These findings reveal that both catalysts have more stability.

Fig. 9a and b shows the adsorption/desorption isotherm and BJH plot of as-made $BaWO_4/CdMoO_4$ nanocomposites with and without glucose to evaluate their pore volume and surface area. Fig. 9b reveals broad pore size distribution with maximum around pores of 64 nm diameter. The total pore volume and average pore diameter for this sample were measured to be 0.06164 cm^3/g and 21.54 nm, respectively. Moreover, the BET analysis was found to be 13.781 m2/g specific surface areas. The surface of the prepared composition in the presence of glucose increased, whereas its size decreased as shown in Fig. 9. Based on the IUPAC classifications, the N_2 adsorption/desorption isotherm belongs to type IV isotherms with H1-type hysteresis loops, that is the substantial features for ordered mesophorous materials. The pore of size distribution for $BaWO_4/CdMoO_4$ nanocomposites has been depicted in Fig. 9b, which demonstrates broad pore size distribution with maximum around pores of 10.57 nm diameter. The total pore volume and mean pore diameter for this sample was computed approximately 0.3136 cm^3/g and 11.431 nm, respectively, and the BET analysis was found to be 122.22 m^2/g specific surface areas. Hence, one can conclude that the use of capping agent in the synthesis of nanoparticles can lead to decreased size and increased surface area of nanoparticles Table 2).

The optical properties of the $BaWO_4/CdMoO_4$ nanocomposites were characterized by photoluminescence (PL) spectroscopy. Room temperature PL spectrum of as-obtained samples excited at 350 nm is presented in Fig. 10. The PL spectrum of the $BaWO_4$ shows a blue maximum emission around 521 nm as shown in Fig. 10. The PL spectrum of $BaWO_4/CdMoO_4$ nanocomposites is around 537 nm as shown in Fig. 10. The red-shift observed in the $BaWO_4/CdMoO_4$ nanocomposites compared to $BaWO_4$, could be due to the possible presence of the $CdMoO_4$. Another interesting effect in PL spectra is the enhancement in the emission for the $BaWO_4/CdMoO_4$ nanocomposites, which can be associated with an inter band connection between the interface of $BaWO_4$ and $CdMoO_4$, where $CdMoO_4$ confines the photo generated electron–hole pairs to the $BaWO_4$ interface which is modified by the quantum confinement effect. This, leads to the passivation of non-radiative transitions, thus enhancing the luminescence

Please cite this article in press as: Eghbali-Arani, M. et al., Optimization and detailed stability study on coupling of $CdMoO_4$ into $BaWO_4$ for enhanced photodegradation and removal of organic contaminant. Arabian Journal of Chemistry (2018), https://doi.org/10.1016/j.arabjc.2018.05.007

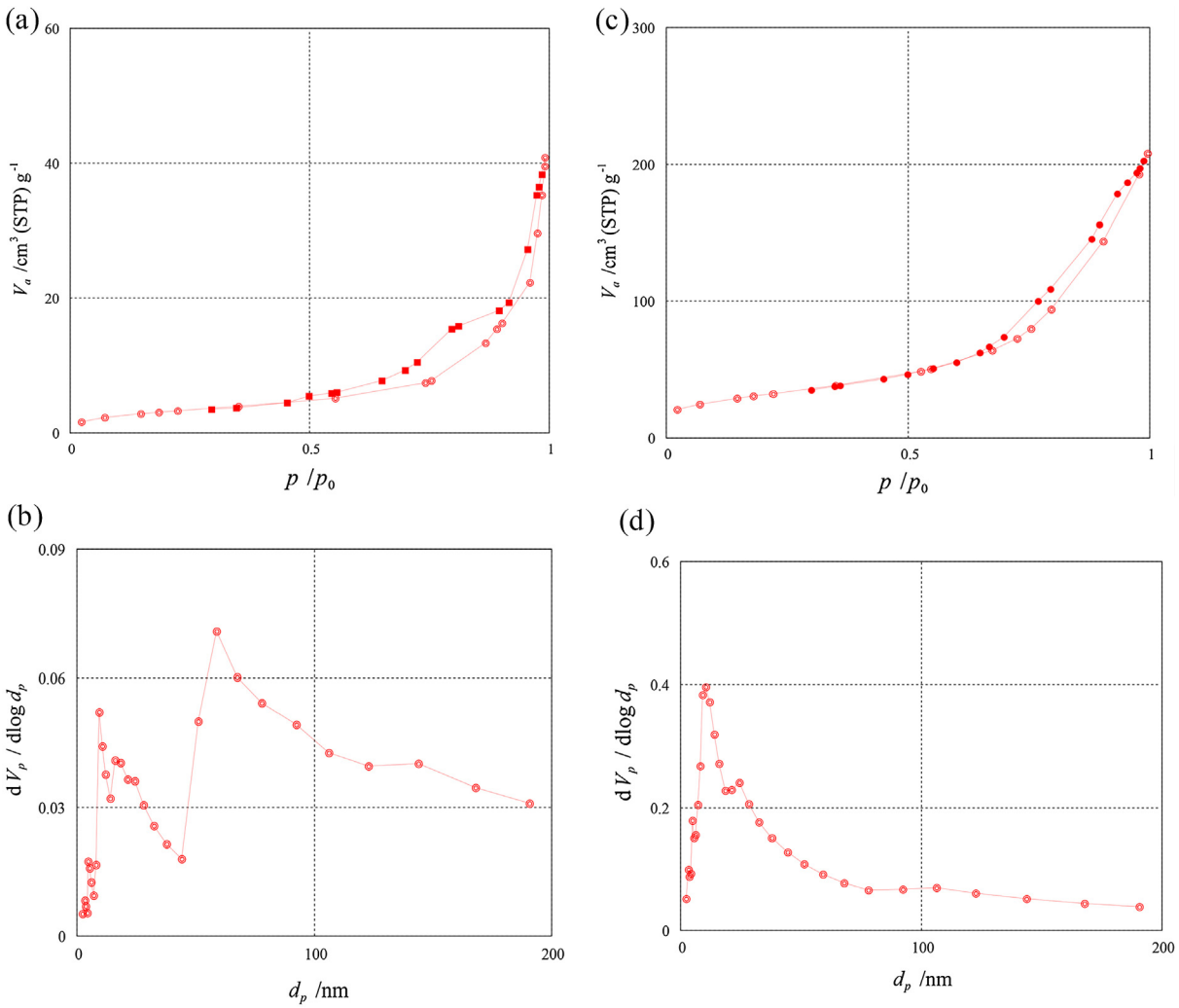

Fig. 9 BET pattern of $BaWO_4/CdMoO_4$ nanocomposites obtained (a,b) without capping agents and (c,d) in the presence of glucose.

Table 2

Sample no	Debye–Scherrer crystallite size (nm)	Capping agents	Total pore volume	Mean pore diameter	Specific surface areas
$BaWO_4/CdMoO_4$	36.7	–	0.06164	21.54	13.781
$BaWO_4/CdMoO_4$	24.6	Glucose	0.3136	11.431	122.22

intensity. Thus, the nanocomposites interface can be directly monitored by PL.

The optical property of nanocomposites, which is related to the electronic structure, can be considered as an important factor to specify the photocatalytic properties. The UV–Vis diffuse reflectance spectra of $BaWO_4$ and $BaWO_4/CdMoO_4$ nanocomposites have been illustrated in Fig. 11 a. The absorption edge for all the samples falls in the visible region (k > 250 nm) which indicates that the entire sample is active at UV-Visible light, with enhanced absorption property observed for $BaWO_4/CdMoO_4$ photocatalyst. The band gaps of the samples were determined from the $[\alpha h\nu]^{1/2}$ versus photon energy (hν) plot as shown in Fig. 11b. It could be noted that each spectrum has two slopes. Therefore extrapolating the linear region of the curve gives the band gap values for $BaWO_4$ and $BaWO_4/CdMoO_4$ as 3.00 eV, and 2.85 eV, respectively. As there is no doping between the metal oxides, the existence of two band gaps in $BaWO_4/CdMoO_4$ could be related to the vast difference in the conduction band energy of the metal oxides.

Recently nanoparticles and nanocomposites are frequently being used as catalysts (Yu et al., 2017; Wang and Zeng, 2017; Zhu et al., 2018b,c,2017a; Pastrana-Martínez et al., 2014; Chen et al., 2018; Wang et al., 2018; Li et al., 2018). Photocatalytic activities of $BaWO_4$ and $BaWO_4/CdMoO_4$ nanocomposites have been investigated under visible light irradiation. In Fig. 12 we have shown photocatalytic reactions for Rh B in solution with various pH levels. As one can expect, the

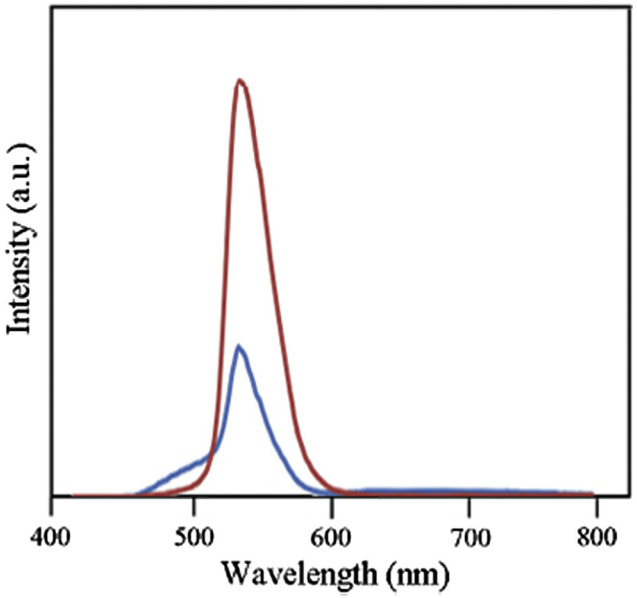

Fig. 10 Room temperature PL spectra of $BaWO_4$ nanostructures and $BaWO_4/CdMoO_4$ nanocomposites.

photocatalytic activity was improved with increase in the value of pH. It has been proposed that the impact of solution pH on the photocatalytic degredation is a complex subject, which is related to the adsorption characteristics of substrate onto photocatalyst surface and reaction mechanism. Based on the principle of heterogeneous photocatalysis, the concentration of $HO^{\cdot}$ ions can be considered as a crucial factor for the generation of $HO^{\cdot}$ radicals. Hence, at higher pH value, the formation of hydroxyl ion was preferred. However, it should be emphasized that the lifetime of $HO^{\cdot}$ radicals is very short and photocatalytic reactions can only take place at or near the surface of photocatalyst. Thank to the non-ion property of Rh B, the neutral medium seems to be advantageous for the absorption of Rh B. Consequently, considering the combined influence of generation of OH and the interaction between surface of photocatalyst and Rh B, the photocatalytic degradation of Rh B was highly effective in neutral medium (Sobhani-Nasab et al., 2015).

Based on Fig. 13a, $BaWO_4$ (sample No. 1) can destruct only 60.3% of Rh B pollutant, whereas destruction of this pollutant in $BaWO_4/CdMoO_4$ nanocomposites (sample No. 2) can peak at 98%. Therefore, $BaWO_4$ had substantial influence on photocatalytic activity of $CdMoO_4$. Interestingly, $BaWO_4$ nanoparticles can contribute to a red shift in nanocomposites, which caused reduce in band gap and more adsorption in visible light. Moreover, it is suggested that, adding $CdMoO_4$ may give rise to appropriate distribution of $BaWO_4$, facileness of the absorption of Rh B pollutant, and its transition to the active sites on $BaWO_4$, and further separation of charge carrier as well. Therefore, it can cause the enhancement in destruction efficiency of $BaWO_4$ to Rh B pollutant. Thus, introducing $CdMoO_4$ can enhance effectiveness of $BaWO_4$ (Huang et al., 2014; Zinatloo-Ajabshir et al., 2017).

Fig. 13a demonstrates effects of various capping agents on the photocatalytic behavior of $BaWO_4/CdMoO_4$ nanocomposites (samples 6–9). Additionally, compounds with the Ba^{2+} to

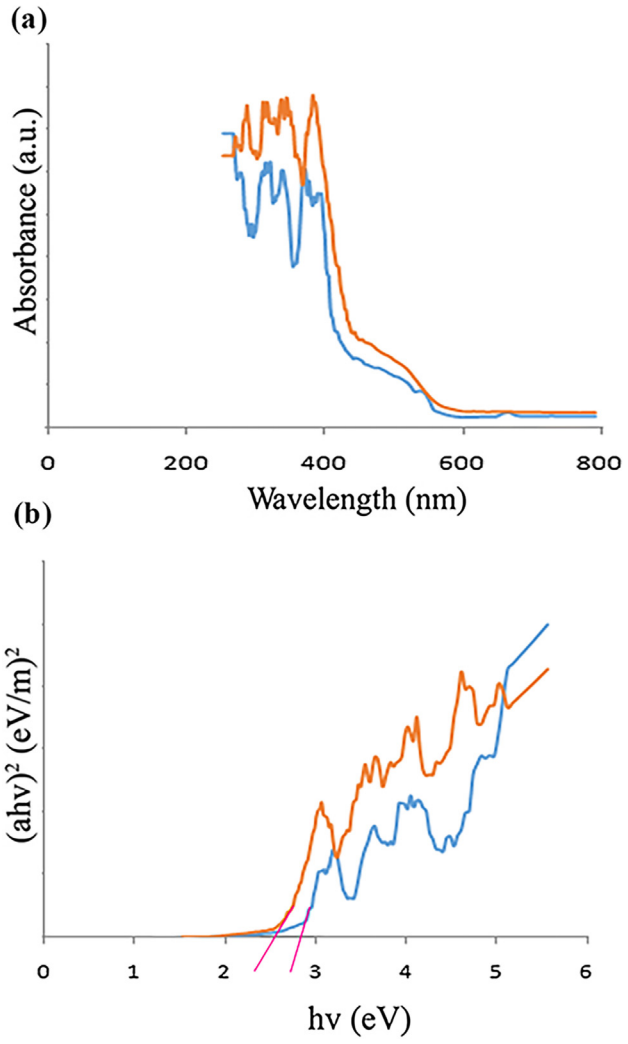

Fig. 11 UV–vis diffuse reflectance spectrum (a) of the as prepared $BaWO_4$ nanostructures and $BaWO_4/CdMoO_4$ nanocomposites (sample No. 1) and (b) Tauc plot pattern $BaWO_4$ nanostructures and $BaWO_4/CdMoO_4$ nanocomposites (sample No. 7).

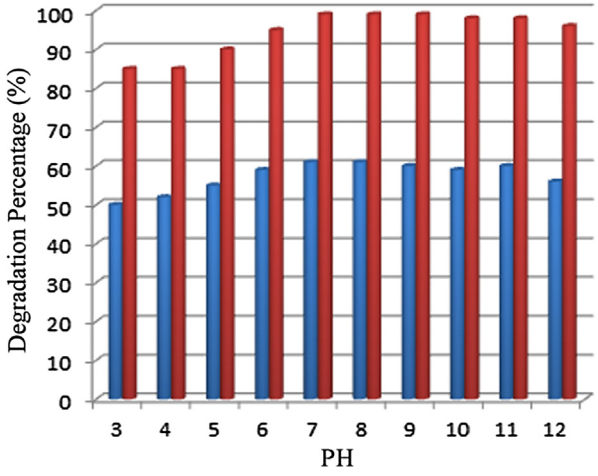

Fig. 12 The influence of the various pH on the Rh B destruction percentage (samples No. 7).

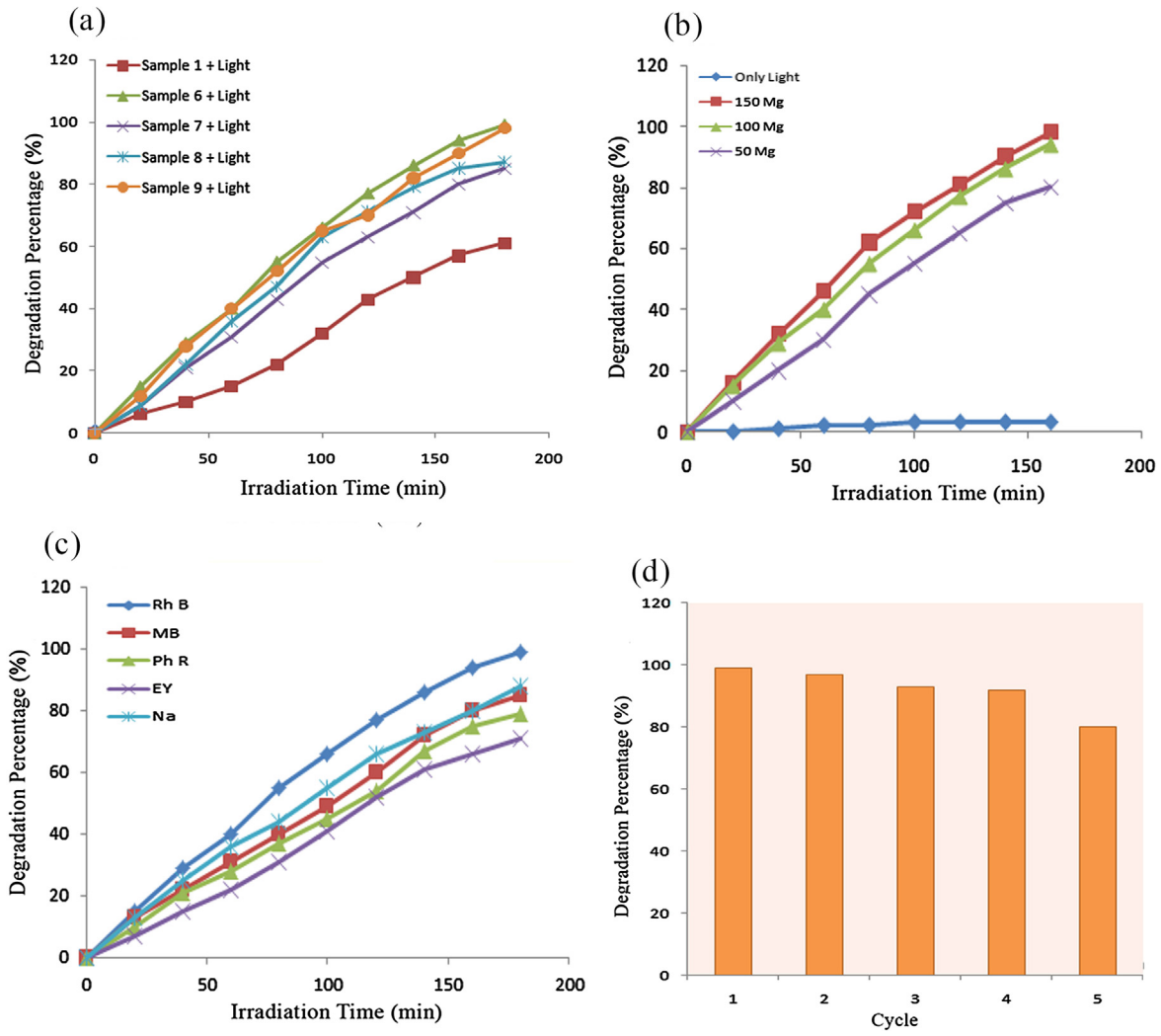

Fig. 13 (a) The photocatalytic behavior of $BaWO_4$ nanostructures (sample No. 1) and $BaWO_4/CdMoO_4$ nanocomposites (sample No. 2), (b) the influence of the dosage of the $BaWO_4/CdMoO_4$ nanocomposites on the Rh B destruction percentage (samples No. 6), (c) the photocatalytic behavior of $BaWO_4/CdMoO_4$ nanocomposites (sample No. 7) on decomposition of various contaminants (cationic and anionic types), and (d) effects of the reuse of the $BaWO_4/CdMoO_4$ nanocomposites on the degradation efficiency of RhB (sample No. 7).

capping agent molar ratio (1:2), have higher photocatalytic degradation. Moreover, fabricated nanocomposites with the capping agent of glucose (sample No. 6) and degradation rate of 99%, demonstrated the most appropriate outcome for the photocatalytic test.

Blank test, Fig. 13a, was carried out in the absence of catalyst to examine the stability of Rh B under visible light. The efficiency of blank test was 4%, which showed a comparatively good stability. The effect of $BaWO_4/CdMoO_4$ nanocomposites concentration on the Rh B destruction has been shown in Fig. 13b. Based on Fig. 13b, the quantities of samples are positively correlated with the percentage of destruction. The destruction rate for 50, 100, and 150 mg of nanocomposites (sample No 7) were 80, 94, and 98%, respectively. Thanks to an insignificant difference between photocatalytic activity of 100 and 150 mg of samples, only 4 percent, and tangible dissimilarity of the second and third samples for this behavior, 15 percent, the appropriate and optimum value for $BaWO_4/CdMoO_4$ nanocomposites, were chosen to be 100 mg.

The photocatalytic degradation of four various dyes, rhodamine B (Rh B), 2-naphthol (Na), methylene blue (MB), phenol red (Ph R), and eosin Y (EY) in the presence of $BaWO_4/CdMoO_4$ nanocomposites was examined under visible irradiation Fig. 13c). Looking at this figure, one can find out that photocatalytic activity of nanocomposites in decolouration of Rh B is more than other dyes. The photocatalytic efficiencies of Rh B, Na, MB, Ph R and EY are 99%, 88%, 85%, 79%, and 71%, respectively.

In addition, repeated degradation reactions have been carried out to determine the stability of the $BaWO_4/CdMoO_4$ nanocomposites. As illustrated in Fig. 9d, the $BaWO_4/CdMoO_4$ nanocomposites (sample No. 7) did not demonstrate any substantial loss of activity after five consecutive reaction cycles, suggesting the high stability of catalyst. The degradation efficiency decreased to 80% after six cycles. The results of photocatalysis survey clearly disclosed that $BaWO_4/CdMoO_4$ nanocomposites may be applied as a useful and successful photocatalyst under visible light.

Please cite this article in press as: Eghbali-Arani, M. et al., Optimization and detailed stability study on coupling of $CdMoO_4$ into $BaWO_4$ for enhanced photodegradation and removal of organic contaminant. Arabian Journal of Chemistry (2018), https://doi.org/10.1016/j.arabjc.2018.05.007

The visible light induced photocatalytic activities of bare $BaWO_4$ and $BaWO_4/CdMoO_4$ were evaluated via the photocatalytic Rh B degradation. Fig. 9 shows the time-dependent profiles of Rh B degradation in the presence of our catalysts under visible light irradiation. In these figures, all the plots of $(\ln(Ct/C0) = k_{app}t)$ versus time (C is the Rh B concentration at time t and C_0 is the initial Rh B concentration) are mostly linear, proving that the kinetics of photocatalytic Rh B decomposition can be described by the pseudo-first-order Langmuir-Hinshelwood kinetic model. Table 3 presents the apparent first-order rate constant (k) of MB degradation for our catalysts under visible light. It can be seen that bare BaWO4/CdMoO4 sample only operated under UVA light (k = 1.556 h^{-1}) and showed very low activity BaWO4 under visible Table 3.

These results demonstrated a high degree of the $BaWO_4/CdMoO_4$ nanocomposites (sample No. 7) to be employed as a favorable, suitable, and new type of photocatalyst under visible light for elimination of cationic contaminants. The composition procedure of contaminants for the $BaWO_4/CdMoO_4$ nanocomposites has been shown in Scheme 2. Once the surface of catalyst is illuminated with the light energy higher than its band gap energy, the holes (h^+) in the valence band and an electron (e^-) in the conduction band of $BaWO_4/CdMoO_4$ nanocomposites (Eq. (12)) can be formed. The holes (h^+) either operate as an oxidizing agent and directly oxidize the pollutant or react with water to form hydroxyl radicals (Eq. (17)). Simultaneously, the electrons (e^-) in the conduction band acts as a reducing agent and reduce the oxygen adsorbed on the surface of $BaWO_4/CdMoO_4$ nanocomposites (Eq. (17)). The probable mechanism for the photodegradation of dye is presented as following (Zinatloo-Ajabshir and Salavati-Niasari, 2017; Aoudjita and Martinsc, 2018; Zhu et al., 2017b).

$$BaWO_4/CdMoO_4 + h^+ \rightarrow BaWO_4/CdMoO_4^{\cdot} + e_{CB}^{-} + h_{VB}^{+} \quad (12)$$

$$e_{CB}^{-} + h_{VB}^{+} \rightarrow heat\ (unproductive) \quad (13)$$

$$h_{VB}^{+} + dye \rightarrow dye^{\cdot+} \rightarrow oxidative\ degradation\ of\ dye \quad (14)$$

$$h_{VB}^{+} + H_2O \rightarrow H^+ + HO^{\cdot} \quad (15)$$

$$h_{VB}^{+} + HO^{-} \rightarrow HO^{\cdot} \quad (16)$$

$$O_2 + e_{CB}^{-} \rightarrow O_2^{\cdot -} \quad (17)$$

$$O^{2\cdot} + 2H_2O \rightarrow HOO^{\cdot} + 2HO^{-} \quad (18)$$

$$2HOO^{\cdot} + H_2O + e_{CB}^{-} \rightarrow HOO^{\cdot} + 2HO^{-} \quad (19)$$

Table 3

Sample no	Debye–Scherrer crystallite size (nm)	Band edge (nm)	Band gap values (eV)	Rate constant of Rh B degradation (h^{-1})	λ maximum emission
$BaWO_4$	21.1	472	3.00	0.0934	521
$BaWO_4/CdMoO_4$	24.6	498	2.85	0.2765	537

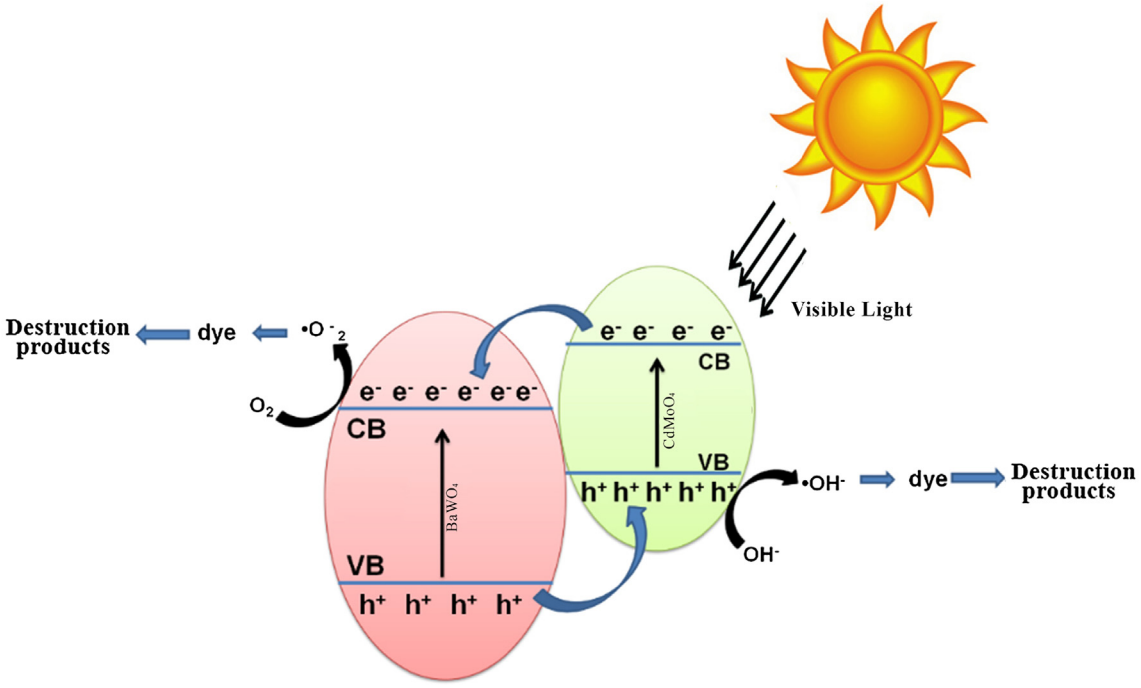

Scheme 2 Schematic illustration of charge transfer in a coupled semiconductor system ($BaWO_4/CdMoO_4$ Nanocomposites).

$$2HOO^{\cdot} + H_2O + e_{CB}{}^{-} \rightarrow H_2O_2 + HO^{-} \quad (20)$$

$$H_2O_2 + e_{CB}^{-} \rightarrow OH + HO \quad (21)$$

$$H_2O_2 + h^{+} \rightarrow 2HO^{\cdot} \quad (22)$$

$$HO^{\cdot} + dye \rightarrow dye\ \ degradation \quad (23)$$

$$O^{2\cdot -} + dye \rightarrow dye\ \ degradation \quad (24)$$

4. Conclusions

The $BaWO_4$ nanoparticles and $BaWO_4/CdMoO_4$ nanocomposites were prepared using green method. To the best of our knowledge, it is the first time that $BaWO_4/CdMoO_4$ nanocomposites are prepared via carbohydrate sugars as a green capping agent. The influence of various carbohydrate sugars including glucose, lactose, fructose, and starch on the shape and size of final products were investigated. Influences of different parameters such as type of dye and light visible on photocatalytic ability of samples were studied. The highest and lowest percentages of degradation of dyes were obtained for Rh B and EY dyes with 99% and 60.3%, respectively. According to the photocatalytic results, one can suggest the high potential of final products for the photocatalytic applications under visible light in degradation of Rh B dye.

Acknowledgment

Authors are grateful to council of University of Kashan and University of Hormozgan for providing financial support to undertake this work. This work was supported by research council of University of Kashan – Iran by Grant Agreement, No. 682151/9.

References

Afanasiev, P., 2007. Molten salt synthesis of barium molybdate and tungstate microcrystals. Mater. Lett. 61, 4622–4626.

Ahmadi, F., Rahimi-Nasrabadi, M., Behpour, M., Ganjali, M.R., 2018. A simple process for the preparation of photocatalytically active bismuth aluminate nanoparticles. J. Mater. Sci.: Mater. Electron. 29, 146–152.

Aoudjita, L., Martinsc, P.M., Madjenea, D.F., Petrovykhe, D.Y., Lanceros-Mendez, S., 2018. Photocatalytic reusable membranes for the effective degradation of tartrazine with a solar photoreactor. J. Hazard. Mater. 344, 408–416.

Chen, P., Dong, F., Ran, M., Li, J., 2018. Synergistic photo-thermal catalytic NO purification of $MnO_x/g\text{-}C_3N_4$: enhanced performance and reaction mechanism. Chin. J. Catal. 39, 619–629.

de Azevedo Marques, A.P., de Melo, D.M.A., Paskocimas, C.A., Pizani, P.S., Joya, M.R., Leite, E.R., Longo, E., 2006. Photoluminescent BaMoO4 nanopowders prepared by complex capping agentization method (CPM). J. Solid State Chem. 179, 671–678.

Dutta, S., Parsons, S.A., Bhattacharjee, C., Jarvis, P., Datta, S., Bandyopadhyay, S., 2009. Kinetic study of adsorption and photodecolorization of Reactive Red 198 on TiO2 surface. Chem. Eng. J. 155, 674–679.

Fan, T.X., Chow, S.K., Zhang, D., 2009. Biomorphic mineralization: from biology to materials. Prog. Mater. Sci. 54, 542–659.

Hosseinpour-Mashkani, S.M., Sobhani-Nasab, A., Mehrzad, M., 2016. Controlling the synthesis $SrMoO_4$ nanostructures and investigation its photocatalyst application. J. Mater. Sci.: Mater. Electron. 27, 5758–5763.

Huang, S.T., Lee, W.W., Chang, J.L., Huang, W.S., Chou, S.Y., Chen, C.C., 2014. Hydrothermal synthesis of $SrTiO_3$ nanocubes: characterization, photocatalytic activities, and degradation pathway. J. Taiwan Inst. Chem. Eng. 45, 1927–1936.

Javidan, A., Ramezani, M., Sobhani-Nasab, A., Hosseinpour-Mashkani, S.M., 2015. Synthesis, characterization, and magnetic property of monoferrite $BaFe_2O_4$ nanoparticles with aid of a novel precursor. J. Mater. Sci.: Mater. Electron. 26, 3813–3818.

Joshi, R., Kumar, P., Gaur, A., et al, 2014. Structural, optical and ferroelectric properties of V doped ZnO. Appl. Nano Sci. 4, 531–536.

Kongsinlark, A., Rempel, G.L., Prasassarakich, P., 2012. Synthesis of monodispersed polyisoprene–silica nanoparticles via differential microemulsion capping agentization and mechanical properties of polyisoprene nanocomposite. Chem. Eng. J. 193, 215–226.

Li, X., Zhang, W., Cui, W., Sun, Y., Jiang, G., Zhang, Y., Huang, H., Dong, F., 2018. Bismuth spheres assembled on graphene oxide: Directional charge transfer enhances plasmonic photocatalysis and *in situ* DRIFTS studies. Appl. Catal. B 221, 482–489.

Mi, Y., Huang, Z.Y., Hu, F.L., Li, X.Y., 2009. Room temperature reverse-microemulsion synthesis and photoluminescence properties of uniform BaMoO4 submicro-octahedra. Mater. Lett. 63, 742–744.

Ozer, D., Dursun, G.B., Ozer, A., 2007. ethylene blue adsorption from aqueous solution by dehydrated peanut hull. J. Hazard. Mater. 144, 171–179.

Pastrana-Martínez, L.M., Morales-Torres, S., Likodimos, V., Falaras, P., Figueiredo, J.L., Faria, J.L., Silva, A.M.T., 2014. Role of oxygen functionalities on the synthesis of photocatalytically active graphene–TiO_2 composites. Appl. Catal. B 158, 329–340.

Pupp, C., Yamdagni, R., Porter, R.F., 1969. Mass spectrometric study of the evaporation of BaMoO4 and BaWO4. J. Inorg. Nucl. Chem. 31, 2021–2029.

Ryu, J.H., Yoon, J.W., Lim, C.S., Shim, K.B., 2005. Microwave-assisted synthesis of barium molybdate by a citrate complex method and oriented aggregation. Mater. Res. Bull. 40, 1468–1476.

Safardoust-Hojaghan, H., Salavati-Niasari, M., 2017. Degradation of methylene blue as a pollutant with N-doped grapheme quantum dot/titanium dioxide nanocomposite. J. Clean. Prod. 148, 31e36.

Sathishkumar, P., Sweena, R., Sambandam Anandan, W.U., 2011. Synthesis of CuO-ZnO nanophotocatalyst for visible light assisted degradation of a textile dye in aqueous solution. Chem. Eng. J. 171, 136–140.

Sobhani-Nasab, A., Rangraz-Jeddy, M., Avanes, A., Salavati-Niasari, M., 2015. Novel sol–gel method for synthesis of $PbTiO_3$ and its light harvesting applications. J. Mater. Sci.: Mater. Electron. 26, 9552–9560.

Sobhani-Nasab, A., Maddahfar, M., Hosseinpour-Mashkani, S.M., 2016. $Ce(MoO_4)_2$ nanostructures: synthesis, characterization, and its photocatalyst application through the ultrasonic method. J. Mol. Liq. 216, 1–5.

Sobhani-Nasab, A., Zahraei, Z., Akbari, M., Maddahfar, M., Hosseinpour-Mashkani, S.M., 2017. Synthesis, characterization, and antibacterial activities of $ZnLaFe_2O_4/NiTiO_3$ nanocomposite. J. Mol. Struct. 1139, 430–435.

Sun, Y., Ma, J., Fang, J., Gao, C., Liu, Z., 2011. Effect of MgO/CaO ratio on the microstructure of cordieritebased glass-ceramic glazes for floor tiles. Ceram. Int. 31, 683–686.

Wang, H., Sun, Y., Jiang, G., Zhang, Y., Huang, H., Wu, Z., Lee, S. C., Dong, F., 2018. Unraveling the mechanisms of visible light photocatalytic NO purification on earth-abundant insulator-based core-shell heterojunctions. Environ. Sci. Technol. 52, 1479–1487.

Wang, C., Zeng, W., 2017. New insights into multi-hierarchical nanostructures with size-controllable blocking units for their gas sensing performance. J. Mater. Sci.: Mater. Electron. 28, 10847–10852.

Wei, S., Chen, Y., Ma, Y., et al, 2010. Fabrication of CuO/ZnO composite films with cathodic co-electrodeposition and their photocatalytic performance. J. Mol. Catal. A Chem. 331, 112–116.

Xia, C.T., Fuenzalida, V.M., Zarate, R.A., 2001. Electrochemical preparation of crystallized Ba1-x$Sr_x$$MoO_4$ solid-solution films at room-temperature. J. Alloy Compd. 316, 250–255.

Yu, Y., Xia, Y., Zeng, W., Liu, R., 2017. Synthesis of multiple networked NiO nanostructures for enhanced gas sensing performance. Mater. Lett. 206, 80–83.

Zhang, C., Shen, E.H., Wang, E.B., Kang, Z.H., Gao, L., Hu, C.W., Xu, L., 2006. One-step solvothermal synthesis of high ordered BaWO4 and BaMoO4 nanostructures. Mater. Chem. Phys. 96, 240–243.

Zhong, J.B., Li, J.Z., Feng, F.M., Lu, Y., Zeng, J., Hu, W., Tang, Z., 2012. Improved photocatalytic performance of SiO2–TiO2 prepared with the assistance of SDBS. J. Mol. Catal. A: Chem. 357, 101–105.

Zhu, S., Li, L., Liu, J., Wang, H., Wang, T., Zhang, Y., Zhang, L., Ruoff, R.S., Dong, F., 2018c. Structural directed growth of ultrathin parallel birnessite on β-MnO_2 for high-performance asymmetric supercapacitors. ACS Nano 12, 1033–1042.

Zhu, L., Li, Y., Zeng, W., 2018a. Hydrothermal synthesis of hierarchical flower-like ZnO nanostructure and its enhanced ethanol gas-sensing properties. Appl. Surf. Sci. 427, 281–287.

Zhu, S., Lu, L., Zhao, Z., Wang, T., Liu, X., Zhang, H., Dong, F., Zhang, Y., 2017a. Mesoporous Ni-doped δ-Bi_2O_3 microspheres for enhanced solar-driven photocatalysis: a combined experimental and theoretical investigation. J. Phys. Chem. C 121, 9394–9401.

Zhu, L., Zeng, W., Ye, H., Li, Y., 2018b. Volatile organic compound sensing based on coral rock-like ZnO. Mater. Res. Bull. 100, 259–264.

Zhu, Y., Zheng, G., Dai, Z., Zhang, L., Ma, Y., 2017b. Photocatalytic and luminescent properties of $SrMoO_4$ phosphors prepared via hydrothermal method with different stirring speeds. J. Mater. Sci. Technol. 33, 23–29.

Zinatloo-Ajabshir, S., Salavati-Niasari, M., Zinatloo-Ajabshir, Z., 2017. Facile size-controlled preparation of highly photocatalytically active praseodymium zirconate nanostructures for degradation and removal of organic pollutants. Sep. Purif. Technol. 177, 110–120.

Zinatloo-Ajabshir, S., Mortazavi-Derazkola, S., Salavati-Niasari, M., 2017. Sonochemical synthesis, characterization and photodegradation of organic pollutant over Nd_2O_3 nanostructures prepared via a new simple route. Separ. Purificat. Technol. 178, 138–146.

Zinatloo-Ajabshir, S., Salavati-Niasari, M., 2017. Photo-catalytic degradation of erythrosine and eriochrome black T dyes using $Nd_2Zr_2O_7$ nanostructures prepared by a modified Pechini approach. Sep. Purif. Technol. 179, 77–85.

Please cite this article in press as: Eghbali-Arani, M. et al., Optimization and detailed stability study on coupling of $CdMoO_4$ into $BaWO_4$ for enhanced photodegradation and removal of organic contaminant. Arabian Journal of Chemistry (2018), https://doi.org/10.1016/j.arabjc.2018.05.007